JMEPEG (2019) 28:3186–3195
https://doi.org/10.1007/s11665-019-03896-5

1059-9495/$19.00

Study of the Effects of Materials Selection for the Closeout Structure on the Service Life of a Liquid Rocket Engine Thrust Chamber

M. Ferraiuolo and A. Riccio

(Submitted July 30, 2018; in revised form December 6, 2018; published online February 12, 2019)

The external structure of rocket engines thrust chambers for aerospace applications should be designed in order to provide adequate stiffness to the thrust chamber; however, it affects in a significant way the engine service life since it acts as a structural bound for the internal structure which is subjected to very high temperature values. The adoption of thin closeout structures allows to have lighter structures and to significantly increase the service life of the thrust chamber. The aim of the present work is to perform numerical investigations on the influence of the closeout geometry and materials on the number of cycles to failure of the thrust chamber. Furthermore, a study on the impact of creep phenomenon on the service life is illustrated. In particular, the present paper is focused on the thermomechanical study of the closeout structure, in terms of material choice, thickness, joining process with the inner liner, etc. Transient thermal and static structural nonlinear analyses are conducted by means of a commercial finite element code (ANSYS), in order to evaluate the number of cycles to failure for the investigated configurations. Viscoplastic models are adopted in order to simulate the highly nonlinear and rate-dependent phenomena occurring in the inner liner structure.

Keywords regenerative cooling, service life, thermal ratcheting, thrust chamber

1. Introduction

The aim of the Hyprob project, financed by MIUR (Italian Ministry of University and Research) and leaded by CIRA (Italian Aerospace Research Centre), is to design, manufacture and test a 30 kN thrust chamber based on a regenerative cooling system which adopts liquid methane as refrigerant. The adoption of regeneratively cooled thrust chambers for aerospace applications is necessary when high heat fluxes coming from the combustion chamber are detected. In fact, in order to avoid high temperatures and stresses in the liner, the fuel, that is, usually liquid hydrogen or liquid methane, flows in the thrust chamber cooling channels and, then, is introduced in the thrust chamber where it is burnt (see Fig. 1).

One of the major technological challenges when manufacturing the thrust chamber is to connect the inner liner with the closeout structure ensuring an appropriate service life. A common joining process that has been employed in the past is the vacuum brazing one.

It is a joining process used to connect two or more metals by melting a filler metal into the joint; the filler metal is characterized by a lower melting point with respect to the metals to be joined.

However, several experiments have demonstrated that such a process causes significant losses in terms of mechanical properties of the copper alloy (e.g., tensile strength), since the thermal cycles needed during the brazing process are very severe (Ref 1-11); in fact, in order to melt the brazing alloy, very high temperatures (from 800 to 950 °C) are necessary. Then, the resulting tensile strength of the brazed component is usually halved (Ref 12). Furthermore, the brazing process to be developed is very sophisticated and is not repeatable; then, it should be developed every time a new thrust chamber is to be designed. Another joining process that is widely adopted is electrodeposition of copper and nickel. This process does not need severe thermal cycles, and then, no significant tensile strength degradation of the copper alloy inner liner is expected. Several kinds of electrodeposited closeout structures can be found in the literature; for example, Malone et al. (Ref 13) studied and developed electrodeposited copper alloys having competitive mechanical properties with electrodeposited nickel. A closeout with electrodeposited nickel without electrodeposited copper is employed, for example, in the Ariane engine family HM7, VULCAIN and VINCI (Ref 14, 15). Kasper and Notardonato (Ref 16) described a closeout made of fiberglass composite wrapped over an electrodeposited copper closeout to provide hoop strength. The idea was conceived with the aim of having a more compliant closeout structure leading to a longer cyclic life than one with a stiffer nickel closeout. However, no further developments of such a configuration can be found in the literature because of the probable nucleation of cracks in the thin copper layer of the closeout structure. Additionally, the

This article is an invited submission to JMEP selected from presentations at the International Symposium on Dynamic Response and Failure of Composite Materials (Draf2018) held June 12-15, 2018, on the Island of Ischia, Italy, and has been expanded from the original presentation.

M. Ferraiuolo, Structures and Materials Department, Italian Aerospace Research Center (CIRA), Capua, Italy; and **A. Riccio**, Department of Industrial and Information Engineering, Università degli studi della Campania "Luigi Vanvitelli", Aversa, Italy. Contact e-mail: m.ferraiuolo@cira.it.

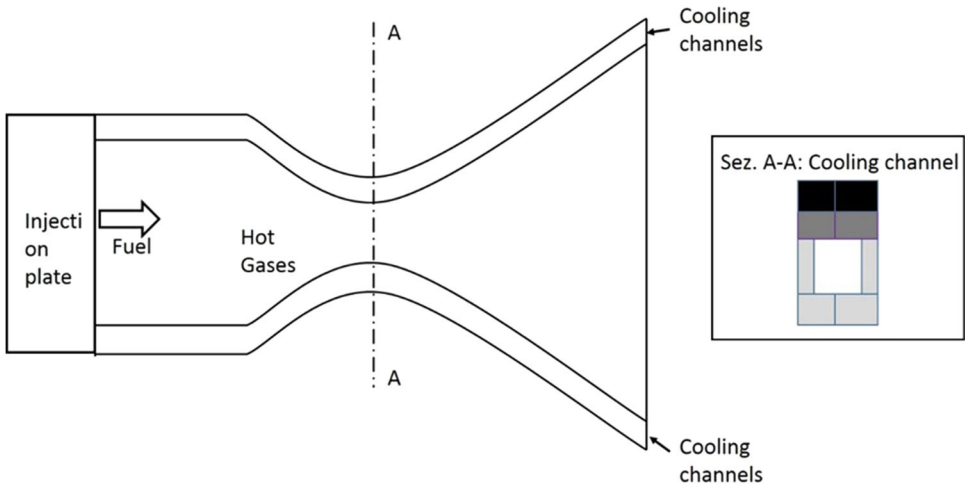

Fig. 1 Scheme of a typical thrust chamber cooling channel

fiberglass composite should be pretensioned during the installation in order to ensure that the fiberglass composite is able to carry the hoop load.

Ferraiuolo et al. demonstrated that a closeout structure made of carbon fiber-reinforced composite could give the possibility to save weight and increase the service life if manufacturing and assembling issues will be solved (Ref 17).

Finally, NASA is also investigating the possibility to develop new processes with nano-structured materials able to save weight in the closeout structure while carrying the pressure load coming from the flowing coolant (Ref 18).

Several authors have analyzed thrust chambers with electrodeposited closeouts with the aim of evaluating the service life and to choose the best suited viscoplastic model (Ref 19, 20); on the other hand, very few works focused on the sizing of the closeout structure can be found in the literature.

Then, in the present work, a configuration with electrodeposited copper and nickel closeout is investigated with the aim of identifying the configuration that ensures the maximum number of cycles to failure varying the thickness of the deposited layers. In fact, analyses of thrust chambers with stiff metallic closeouts show that the thermal tensile strain that occurs during the cooling transient has an effect on the total strain range since the closeout acts almost like a clamped boundary condition for the inner copper liner. Then, minimizing the closeout thickness allows the inner liner to expand and shrink with minimal residual stresses in the ligament (Ref 16). The present paper is structured in the following manner: In the next section, the mathematical model considered is depicted, and in the following section, a description of the numerical model adopted is given; then, the results of the thermostructural analyses conducted on a finite element simplified symmetric model, which represents a cooling channel, are illustrated and discussed. Finally, the conclusive remarks of the present paper are shown.

2. Mathematical Model

2.1 Heat Conduction Model

The thermal transient nonlinear analyses of the cooling channel are performed by means of a finite element commercial code (ANSYS). The heat conduction problem is governed by the following differential equation (Ref 21):

$$\nabla^2 T = \frac{1}{a}\frac{\partial T}{\partial \theta} \quad \text{(Eq 1)}$$

where a is the thermal diffusivity, T is the temperature and θ is the time. The thermal problem is nonlinear since thermal properties are temperature dependent.

Since different materials are in thermal contact (copper alloy, electroformed copper and electroformed nickel), temperature and heat flux continuity conditions are applied at the interface between generic materials i and j:

$$k_i \frac{\partial T_i}{\partial n} = k_j \frac{\partial T_j}{\partial n} \quad \text{(Eq 2)}$$

$$T_i = T_j \quad \text{(Eq 3)}$$

Convective boundary conditions are applied to take into account the effects of the hot gases of the combustion chamber and the effects of the coolant flow:

$$-k\frac{\partial T}{\partial n} = h(T_w - T_\infty) \quad \text{(Eq 4)}$$

where h is a convective heat transfer coefficient, T_w is the wall temperature and T_∞ is the adiabatic wall temperature.

2.2 Structural Model

The equilibrium equation is expressed as follows (Ref 22):

$$\sigma_{ij,i} + X_i = 0 \quad \text{(Eq 5)}$$

where σ_{ij} is the Cauchy stress tensor, while X_i represents the body force per unit volume. The elastic equilibrium equation must be combined with the compatibility equations, the constitutive laws (where the strain tensor is a linear function of the stress tensor) and the relationship between the strain tensor and temperature variation with respect to the reference temperature (temperature at which no thermal strain is detected). More specifically, the total strain ε is decomposed into elastic and plastic components:

$$\boldsymbol{\varepsilon}_{ij} = \boldsymbol{\varepsilon}_{ij}^{\mathrm{el}} + \boldsymbol{\varepsilon}_{ij}^{\mathrm{pl}} \quad \text{(Eq 6)}$$

where ε_{ij}^{el} and ε_{ij}^{pl}, respectively, represent the elastic and plastic components (Ref 23-26).

The viscoplastic model identified adopts the von Mises yield criterion, the bilinear kinematic hardening rule, the Prandtl–Reuss flow rule and, finally, the Norton's law to describe the creep phenomenon; a detailed description of the characteristics of the present viscoplastic model in comparison with other ones can be found in Ref 27.

In general, the yield criterion establishes a relationship among the stresses to predict material yielding, and then, it delineates the surface that separates the elastic stress domain, inside the yield surface, from the plastic stress domain which lies outside the yield surface (Ref 17-20). Plastic strains will be detected when the equivalent stress σ_e equals the yield value σ_y. The yield surface, when kinematic hardening is adopted, can be formulated as follows:

$$F(\boldsymbol{\sigma}, k, \boldsymbol{\alpha}) = 0 \quad \text{(Eq 7)}$$

where k represents the plastic work and $\boldsymbol{\alpha}$ the translation of the yield surface (back stress tensor). In particular, the plastic work is:

$$k = \int \boldsymbol{\sigma}^T [M] \mathbf{d}\boldsymbol{\varepsilon}^{\mathbf{pl}} \quad \text{(Eq 8)}$$

where $[M]$ is a diagonal matrix:

$$[M] = \begin{bmatrix} 1 & 0 & 0 & 0 & 0 & 0 \\ 0 & 1 & 0 & 0 & 0 & 0 \\ 0 & 0 & 1 & 0 & 0 & 0 \\ 0 & 0 & 0 & 2 & 0 & 0 \\ 0 & 0 & 0 & 0 & 2 & 0 \\ 0 & 0 & 0 & 0 & 0 & 2 \end{bmatrix}$$

On the other hand, $\boldsymbol{\alpha}$ is:

$$\boldsymbol{\alpha} = \int C \mathbf{d}\boldsymbol{\varepsilon}^{\mathbf{pl}} \quad \text{(Eq 9)}$$

where C is a material parameter.

The stress–strain relations for a bilinear kinematic hardening model are expressed, when considering a one-dimensional plasticity model, as:

$$\sigma = \begin{cases} E\varepsilon & \text{if } \gamma = 0 \\ \frac{EK}{E+K}\varepsilon & \text{if } \gamma > 0 \end{cases} \quad \text{(Eq 10)}$$

where γ is the absolute value of the plastic strain rate and K is the plastic modulus (Ref 28). In Fig. 2, a visual representation of the kinematic hardening rule is shown.

Then, the flow rule specifies the interdependence occurring between the plastic strain increase and the deviatoric stresses. In this case, the above-mentioned Prandtl–Reuss flow rule expresses a linear relationship between the plastic strain increment and the deviatoric stresses (Ref 24, 25):

$$\mathrm{d}\boldsymbol{\varepsilon}_{ij} = \boldsymbol{S}_{ij} \mathrm{d}\lambda \quad \text{(Eq 11)}$$

where $\mathrm{d}\varepsilon_{ij}$ is the plastic strain increments, S_{ij} is the deviatoric stresses and λ is the plastic multiplier which is evaluated by imposing that the stress state lies on the yield surface during plastic flow.

To conclude, the Norton's law, adopted for primary and secondary creep regimes, defines how the creep strain rate is affected by the stresses (Ref 23):

$$\dot{\boldsymbol{\varepsilon}} = B\boldsymbol{\sigma}^n \quad \text{(Eq 12)}$$

where n and B are material constants. For the copper alloy adopted, the following values have been considered:

$$B = 5.12 * 12^{-56} [1/\mathrm{s}\,(\mathrm{MPa})^{\mathrm{r}}]$$

$$n = 6.65$$

The present viscoplastic model has been mostly adopted to analyze the thermomechanical behavior of the copper alloy liner structure which is exposed to high thermal loads and, then, to high-temperature values in the inner surface of the thrust chamber.

3. Numerical Model

The finite element method has been adopted to solve the partial differential equations illustrated in the previous section. Since the structural problem is nonlinear, a stepwise approach has been adopted to apply the thermomechanical loads. Then, the Newton–Raphson method has been considered to solve every load step. The main assumptions considered for the numerical analyses are:

- One-way coupling between thermal and structural field, that is, the thermal field is solved first, followed by the structural viscoplastic analysis; namely, the temperature field represents a body load for the structural analysis. On the other hand, the displacement/strain field does not have a significant impact on the temperature field, as demonstrated in several works (Ref 29, 30).
- Small deformations, then, a geometrical linear model is adopted.

A detailed description of the steps to be followed during the numerical solution is described next: An Euler backward scheme is adopted to guarantee that the updated stresses and strains lie on the yield surface. Then,

- the yield stress is evaluated (it varies with temperature);
- stresses are calculated considering the trail strain $\boldsymbol{\varepsilon}^{tr}$ (Ref 28):

$$\boldsymbol{\varepsilon}_n^{tr} = \boldsymbol{\varepsilon}_n - \boldsymbol{\varepsilon}_{n-1}^{pl} \quad \text{(Eq 13)}$$

where ε_n represents the total strain and ε_{n-1}^{pl} is the plastic strain evaluated in the previous time instant $(n-1)$. Then, the trial stress is calculated as follows:

$$\boldsymbol{\sigma}_n^{tr} = \boldsymbol{\sigma}_{n-1} + D\boldsymbol{\varepsilon}_n^{tr} \quad \text{(Eq 14)}$$

where D is the elasticity matrix;

- the equivalent stress σ_e is calculated; if the yielding condition is not satisfied, the material behavior is elastic;if bilinear kinematic hardening is considered:

$$\sigma_e = \left[\frac{3}{2}(\boldsymbol{s} - \boldsymbol{\alpha})^T [M] (\boldsymbol{s} - \boldsymbol{\alpha})\right]^{1/2} \quad \text{(Eq 15)}$$

- the plastic strain increment $\Delta\varepsilon_{pl}$ is evaluated according to Eq 11;
- the plastic strain is, then, updated:

$$\boldsymbol{\varepsilon}_n^{pl} = \boldsymbol{\varepsilon}_{n-1}^{pl} + \Delta\boldsymbol{\varepsilon}_{\mathbf{pl}} \quad \text{(Eq 16)}$$

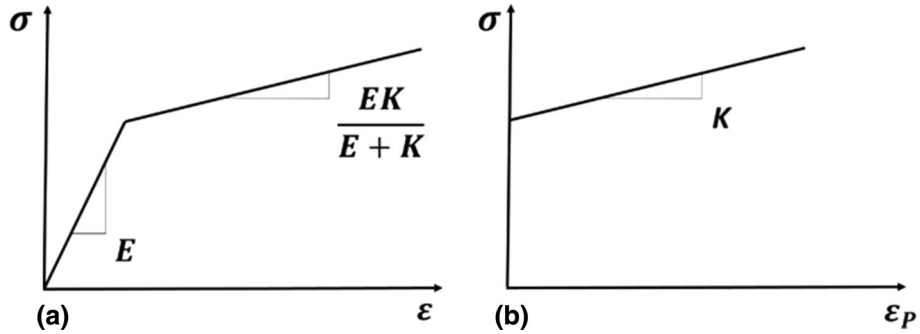

Fig. 2 Stress–strain—kinematic hardening

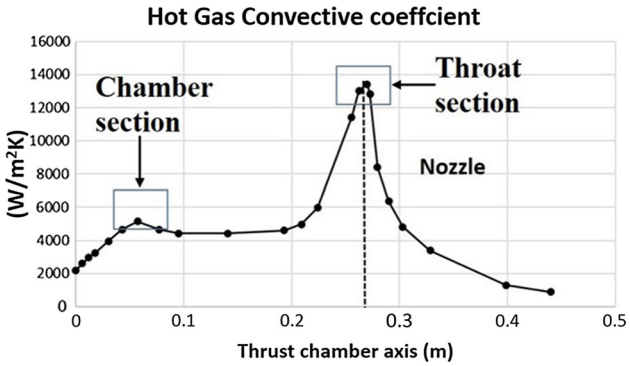

Fig. 3 Heat transfer coefficient profile along the thrust chamber—hot gas side

while the elastic strain is:

$$\varepsilon^{\mathrm{el}} = \varepsilon^{\mathrm{tr}} - \Delta\varepsilon_{\mathbf{pl}} \quad \text{(Eq 17)}$$

And the stress vector is:

$$\boldsymbol{\sigma} = D\varepsilon^{\mathrm{el}} \quad \text{(Eq 18)}$$

- Plastic work k and back stress tensor $\boldsymbol{\alpha}$ increments are evaluated according to Eq 8 and 9.

If rate-dependent plasticity is considered, the equations of creep are integrated with an explicit Euler forward algorithm.

3.1 Boundary Conditions

Half cooling channel is studied taking advantage of the symmetry conditions. The cross sections chosen for the analyses are the throat and the chamber section corresponding to the rectangles in Fig. 3. The geometric parameters illustrated in Fig. 4 are reported in Table 1:

In particular, in the throat sections the maximum heat flux values are expected; then, high-temperature values are envisaged (see Fig. 3). On the other hand, the chamber section corresponding to the left rectangle could be critical from a structural point of view since it is less stiff with respect to the throat section (the ratio between geometric parameters a and b in Fig. 4 is higher). Furthermore, the cooling efficiency of the chamber section channel is considerably lower since the coolant temperature is higher and the heat transfer coefficient is smaller (the section area is significantly higher than that of the throat section, and consequently, the fluid velocity and the heat transfer coefficient are smaller).

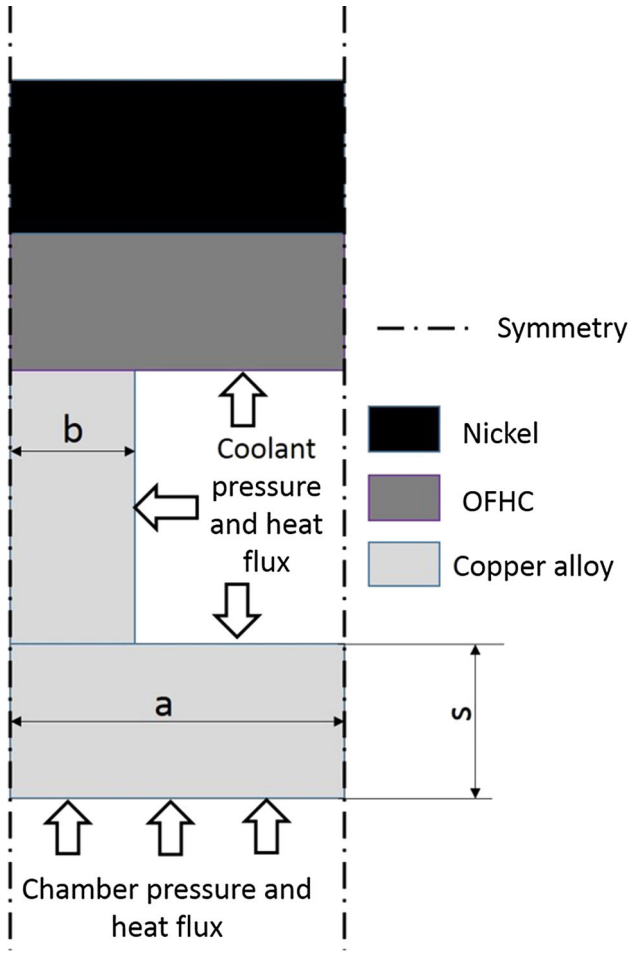

Fig. 4 Boundary conditions

Table 1 Geometric parameters of the cooling channel

	a, mm	*b*, mm	*s*, mm
Chamber	2	0.62	0.9
Throat	1	0.62	0.9

Thermal and structural loads, that is, body temperature distribution in the hot phase and the maximum pressure in the cooling channels, are considered in the finite element model for the structural analyses.

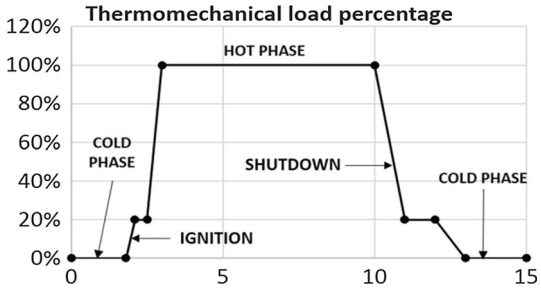

Fig. 5 Thermomechanical cycle

The thermomechanical load cycle adopted is representative of a typical experimental hot fire test which is essentially made of three stages: ignition, hot phase and shutdown. During the ignition phase, the igniter produces a torch flame to ignite the thrust chamber, and then, combustion of the hot gases provokes a significant increase in pressures and temperatures in the combustion chamber, and finally, propellant flow is stopped. The resulting thermomechnical load cycle is illustrated in Fig. 5. In particular, those loads are specified in terms of percentages of the actual load with respect to the maximum loads. The thermal load is represented by the heat fluxes generated by the combustion of the gases, while the mechanical loads are just the pressure of the coolant in the cooling channel and the pressure of the hot gases acting on the inner liner of the combustion chamber. The hot phase lasts from 3 to 10 s of the load cycle, while the cold phase is represented from 0 to 3 s and from 13 to 15 s. Further details on pressure and heat flux laws during a fire test can be found in Ref 11.

Two-dimensional thermostructural analyses have been performed on the cross section of the cooling channel. The results of the computational fluid dynamic (CFD) analyses, described in Ref 31, provide the convective boundary conditions to be applied on the internal surface of the combustion chamber and inside the cooling channel. The initial condition considered for the transient thermal analyses is the room temperature (298 K). The convective heat transfer coefficients and the adiabatic wall temperatures considered in the thermal analyses are summarized in Table 2. The subscripts *hot* and *cold* refer, respectively, to the hot gases and cooling channel sides. The superscripts T and C denote the throat section and the chamber sections (see Fig. 5).

The chamber pressure is 5.5 MPa, while the coolant pressures for the throat section and the chamber section are, respectively, 8.4 MPa and 7.2 MPa. The heat transfer coefficients on the hot gas side and the chamber pressure values are scaled according to Fig. 5.

3.2 Material Properties

The thermal and mechanical properties adopted for the thermostructural analyses can be found in Ref 32. Tables 3, 4, 5, 6, 7 and 8 show the physical and mechanical properties of the copper alloy (CuCrZr), the electrodeposited OFHC and the electrodeposited nickel.

3.3 Finite Element Model

Quadrangular plane elements have been considered for both the thermal and the structural analyses, that is, ANSYS PLANE55 for the thermal model and ANSYS PLANE42 for the structural one (see Fig. 6). Generalized plane strain conditions have been applied for the structural analysis, that is, the normal strain in the z axial direction of the thrust chamber is not assumed to be zero as in the plane strain model, but equal to a constant value:

$$\epsilon_{zz} = \text{constant}$$

Riccius et al. demonstrated that the generalized plane strain model is more realistic than the plane strain one (Ref 25); in fact, since the thermal expansion coefficient of the material is isotropic, the strain in the axial direction is comparable to the strain in the radial and circumferential direction ($\epsilon_{zz} \neq 0$). In particular, the plane strain model is more conservative than the generalized plane strain and three-dimensional model; furthermore, Riccius showed that the results obtained with the generalized plane strain model, in terms of service life, are in good agreement with the results achieved with the three-dimensional model with an obvious significant saving in computational costs.

A trade-off study has been performed by varying the following geometric parameters (see Fig. 6):

- t_1: OFHC deposited copper
- t_2: Deposited nickel

The thermal analyses are always transient, while the structural analyses are static when considering the throat section and transient when considering the chamber section.

As regards the throat section, static structural analyses are performed since transient effects are expected to be irrelevant; on the contrary, the chamber section has been analyzed by means of transient structural analyses because the ligament length is significantly greater than the corresponding value in the throat. As a consequence, transient effects like thermal shocks cannot be neglected.

3.4 Failure Criteria

With regard to the static failure, the von Mises criterion has been adopted, that is, the maximum von Mises stress is compared to the maximum allowable for the material adopted (see Fig. 7).

The relationship to be satisfied for this criterion is:

$$\sigma_{\text{vm}} < \sigma_{\text{UTS}} \qquad \text{(Eq 19)}$$

where σ_{vm} is the von Mises stress and σ_{UTS} is the tensile ultimate stress.

With regard to the quasistatic fatigue evaluations, the service life is computed according to Ref 19:

$$N = \frac{\epsilon_{\text{u}}}{\max(0, \epsilon_e - \epsilon_{\text{b}})} \qquad \text{(Eq 20)}$$

where ϵ_e is the remaining strain after the considered cycle, ϵ_{b} is the strain at the beginning of the considered cycle and ϵ_{u} is the ultimate strain of the combustion chamber wall material. Negative strains (compression mode) are not taken into account. For the application considered in the present work, thermal ratcheting, which represents the progressive increase in inelastic strains in a structure subjected to thermal and mechanical cyclic loading, is the dominant type of failure (Ref 27).

Table 2 Heat transfer coefficients and adiabatic wall temperatures

h^{T}_{hot}, $\frac{W}{m^2 K}$	h^{C}_{hot}, $\frac{W}{m^2 K}$	h^{T}_{cold}, $\frac{W}{m^2 K}$	h^{C}_{cold}, $\frac{W}{m^2 K}$	T^{T}_{hot}, K	T^{C}_{hot}, K	T^{T}_{cold}, K	T^{C}_{cold}, K
13,600	5600	680,000	280,000	3600	3600	300	370

Table 3 Physical properties copper alloy (CuCrZr)

Temperature, K	Density, kg/m^3	Thermal conductivity, W/m K	Specific heat, J/kg K	Thermal expansion coefficient, 1/K
300	8933	320	390	15.7×10^{-6}
600	8933	290	390	17.9×10^{-6}
900	8933	255	400	18.7×10^{-6}

Table 4 Mechanical properties copper alloy (CuCrZr)

Temperature, K	*E*, Gpa	Yield stress, MPa	Ultimate stress, MPa	Elongation at break, %
300	130	433.9	477.9	20
500	106	383.3	402.9	18
700	87	313	329.4	18
900	44	156.3	175.4	22

Table 5 Physical properties electrodeposited OFHC

Temperature, K	Density, kg/m^3	Thermal conductivity, W/m K	Specific heat, J/kg K	Thermal expansion coefficient, 1/K
300	8913	390	385	17.2×10^{-6}

Table 6 Mechanical properties electrodeposited OFHC

Temperature, K	*E*, Gpa	Yield stress, MPa	Ultimate stress, MPa	Elongation at break, %
28	118	68	413	20
294	114	60	208	20
533	65	50	145	20
755	40	38	80	20

Table 7 Physical properties electrodeposited nickel

Temperature, K	Density, kg/m^3	Thermal conductivity, W/m K	Specific heat, J/kg K	Thermal expansion coefficient, 1/K
300	8913	90	444	12.2×10^{-6}

Table 8 Mechanical properties electrodeposited nickel

Temperature, K	*E*, Gpa	Yield stress, MPa	Ultimate stress, MPa
28	193	344	551

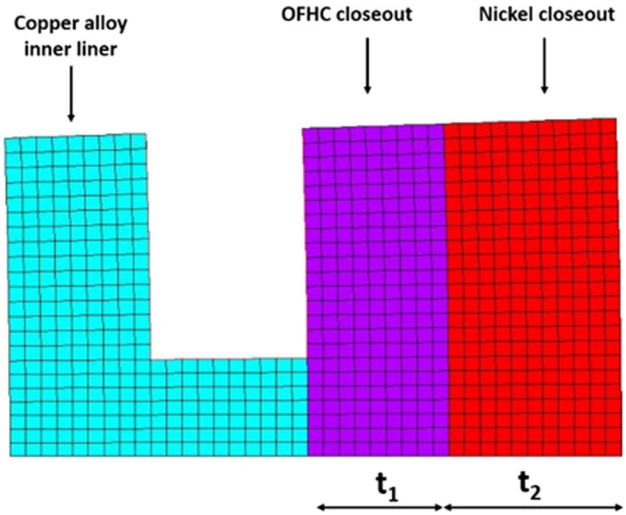

Fig. 6 Finite element model

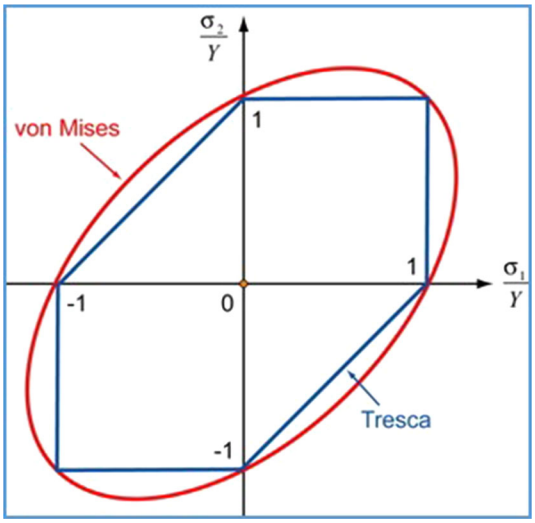

Fig. 7 von Mises stress criterion

4. Results and Discussion

Several thermostructural analyses have been conducted varying t_1 and t_2 from 0.5 to 3 mm. The number of loading cycles considered in the analyses is three; however, it will be demonstrated that this choice leads to a slight underestimation of the number of cycles to failure. In fact, if more cycles are taken into account, since kinematic hardening occurs and increases the yield stress, the plastic strain increase $\Delta\varepsilon^{pl}$ tends to become smaller cycle after cycle. In order to verify this assumption, the service life for the configuration with t_1= 1.5 mm and t_2 = 2 mm has been evaluated considering three and six loading cycles. The results have shown that with three loading cycles the service life is 10% smaller than that calculated with six loading cycles. Then, with the aim of saving computational time, three loading cycles are taken into account for all the configurations.

A grid sensitivity analysis has also been performed in order to verify that the results are not affected by the number of elements considered. Figure 8 shows that changing the number

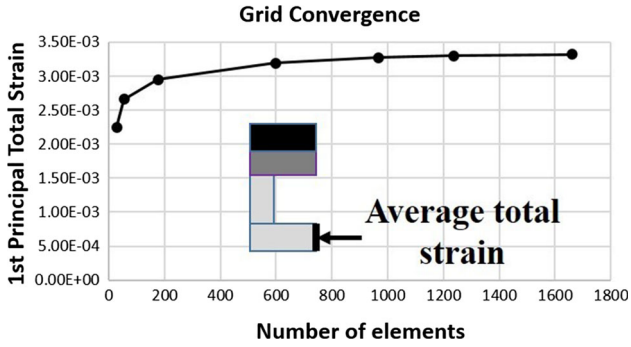

Fig. 8 Service life vs. element size—t_1 = 1 mm; t_2 = 2 mm

Table 9 Number of cycles to failure for the configurations analyzed

	t_1 = 0.5 mm	t_1 = 1 mm	t_1 = 1.5 mm	t_1 = 2 mm
t_2 = 0.5 mm	78	70	68	65
t_2 = 1 mm	85	79	75	74
t_2 = 1.5 mm	88	82	80	79
t_2 = 2 mm	88	83	81	80
t_2 = 2.5 mm	84	81	80	79
t_2 = 3 mm	68	69	69	69

of elements from about 1200 to 1650, the average total strain in the ligament thickness (evaluated at the end of the first cycle) does not significantly change (2%), while considerable differences are detected when the mesh is coarser.

In Table 9, the estimated number of cycles to failure is reported for all the configurations analyzed.

The following configurations:

1. t_1= 0.5 mm; t_2= 2.0 mm
2. t_1= 0.5 mm; t_2= 1.5 mm

are characterized by the highest values of number of cycles to failure. Table 9 clearly shows that the increase in nickel closeout thickness has a beneficial effect on the service life up to 2 mm; beyond this value, a detrimental effect, even though very small, appears. More specifically, two main effects can be detected when the closeout structure becomes thicker:

- increase in the plastic strains, since it acts as a structural bound on the inner copper alloy structure,
- increase in the structural stiffness that allows to avoid excessive deformations in the ligament.

Then, to conclude, the former effect becomes dominant when considering thickness values of the electrodeposited nickel greater than 2 mm, while the latter is clearly the governing effect for smaller t_2 values.

On the other hand, the increase in electrodeposited copper thickness always leads to a decrease in service life; however, the results show that when $t_2 \geq 2$ mm, the influence of t_1 on the service life becomes negligible.

Creep becomes significant when high temperatures are detected, that is, during the hot phase where compressive stresses are encountered. Creep relaxation occurs in the

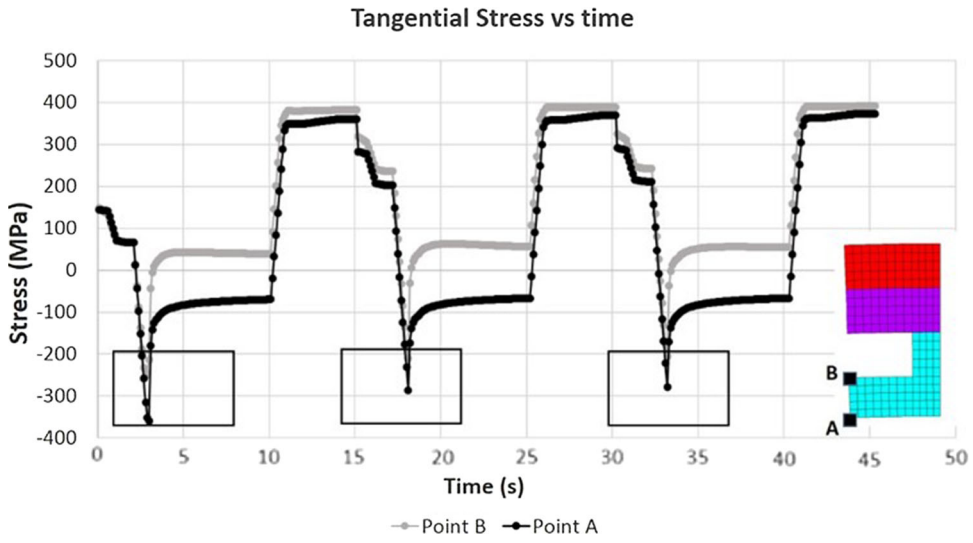

Fig. 9 Tangential stress vs. time—points A and B

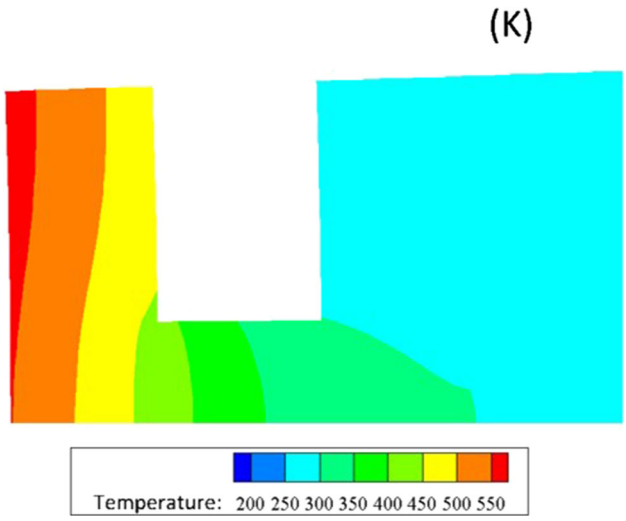

Fig. 10 Temperature contour plot: hot phase

ligament and causes a fast decrease in the compressive stress values. In Fig. 9 (see the black rectangles highlighting the creep effects), which shows how the tangential stress in the ligament changes with time, it is clearly visible that creep relaxation occurs in the first few seconds of the hot phase; then, an increase in the hot phase duration does not affect the service life of the thrust chamber. The creep relaxation time, namely the time needed to reach the stress steady state when creep effects are considered, is strongly influenced by the pressures applied in the thrust chamber and in the cooling channel as demonstrated by Porowski et al. (Ref 33). Then, in the present case, the thrust chamber pressure is responsible for a very short relaxation time.

In order to understand the impact of creep on the service life of the thrust chamber, a thermostructural analysis performed on the best suited configuration neglecting creep effects has shown that if creep is not modeled, the number of cycles to failure is significantly overestimated; in fact, the service life is 465 cycles, that is, more than five times that evaluated considering creep effects (see Table 9).

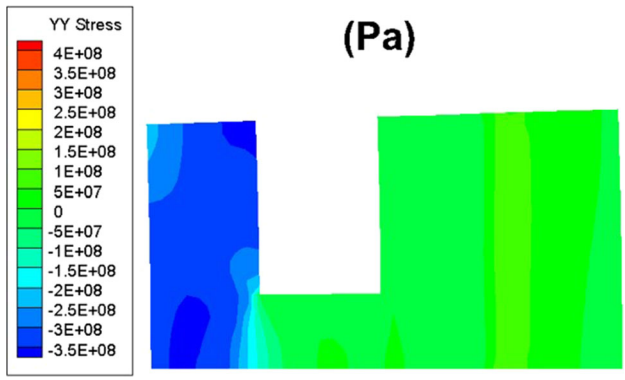

Fig. 11 Tangential stress first cycle: hot phase

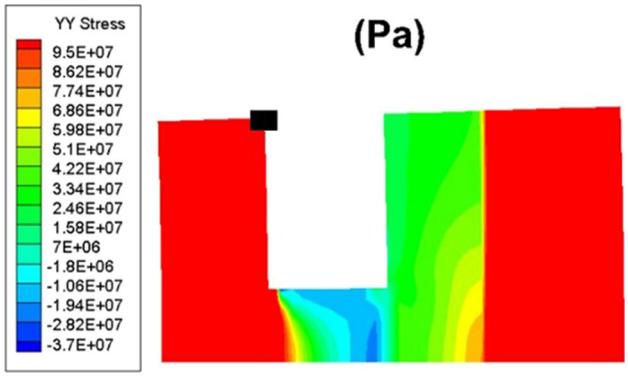

Fig. 12 Tangential stress third cycle: cold phase

Since the type of failure detected for both the chamber and throat sections is thermal ratcheting, then, for the sake of simplicity, only the thermostructural results obtained on the cylindrical part of the thrust chamber are shown. Temperature contour plot in the hot phase is illustrated in Fig. 10. Maximum temperature value is 573 K.

In what follows, the contour plots of the tangential stress detected in the hot phase of the first cycle are shown (Fig. 11).

As expected, significant compressive stresses can be detected during the hot phase of the thermomechnical cycle, while in the cold phase residual tangential stresses (Fig. 12) and, then, tensile plastic strains arise.

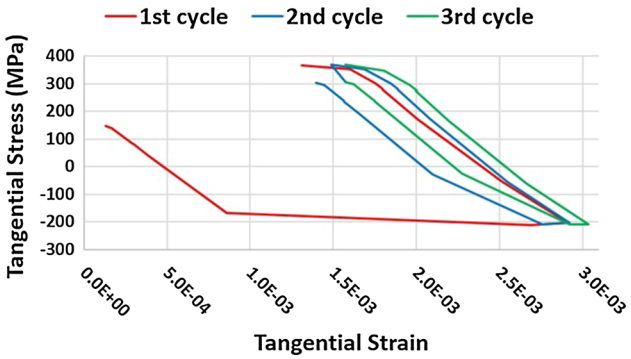

Fig. 13 Tangential stress vs. tangential strain in the ligament

Figure 10 shows the variation of the tangential stress with respect to the tangential strain. The results refer to the area highlighted by the black rectangle in Fig. 13. Thermal ratcheting is the dominant failure phenomenon in this case since the tangential strain increases cycle after cycle.

Figure 14 and 15 shows the margin of safety in the inner liner in the hot and in the cold phase. It is clearly visible that the hot phase is the most critical one and that the ligament is characterized by the lowest margins of safety as expected.

Finally, the results have proved that the chosen configuration is not critical from a thermal and structural point of view.

5. Conclusions and Future Activities

The previous study has demonstrated that when brazing process is adopted between the inner liner and the closeout structures of the thrust chamber, structural criticalities could occur. Then, other joining techniques characterized by less

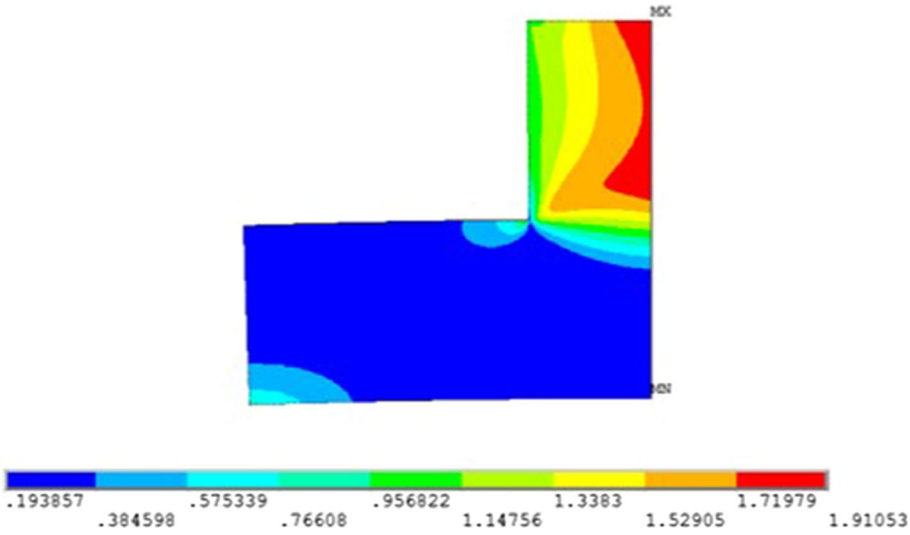

Fig. 14 Margin of safety—hot phase—first cycle—inner liner

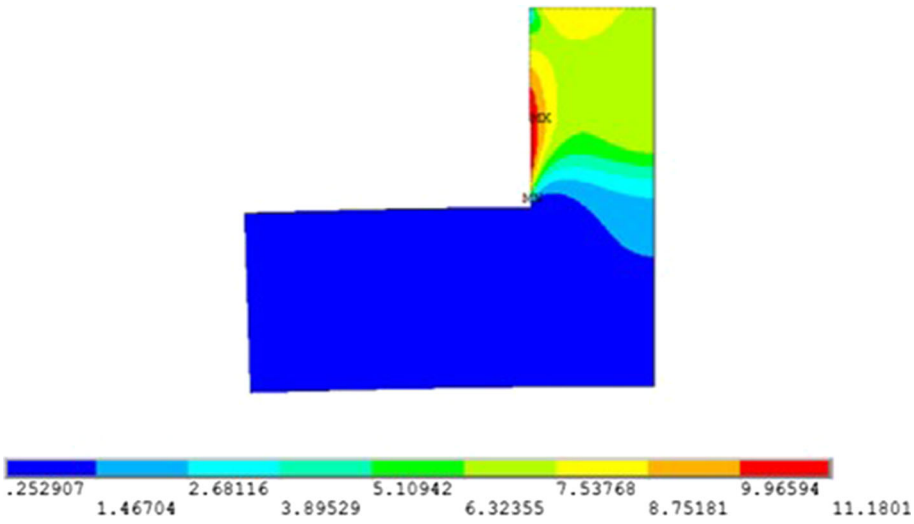

Fig. 15 Margin of safety—cold phase—first cycle—inner liner

critical thermal treatments should be investigated. In the current work, a trade-off analysis has been carried out on the closeout thickness of a regeneratively cooled thrust chamber. The closeout is made of a layer of oxygen-free high-conductivity electrodeposited copper and a layer of electrodeposited nickel. The results of the analyses have shown that the configuration with 0.5 mm of OFHC copper and 1.5 mm of nickel ensures the maximum number of cycles to failure.

The numerical analyses have demonstrated that time-dependent viscoplastic phenomenon, such as creep, has a considerable impact on the service life of the thrust chamber; in fact, the number of cycles to failure is more than five times smaller if compared to those obtained when creep is not considered. Results have also demonstrated that creep induces a relaxation of the compressive stresses in the very few seconds of the hot phase; then, larger duration of hot phase will not lead to a decrease in service life.

The type of failure that is envisaged is thermal ratcheting since tensile plastic strain accumulates cycle after cycles in the copper ligament. Optimization of these configurations is very useful since it could give the possibility to save weight and manufacturing costs. In order to take into account the three-dimensional effects, thermostructural analyses are currently on going; moreover, the authors are studying and trying to implement more detailed viscoplastic models with the aim of having a better representation of the thermomechanical behavior of the cooling channel. Finally, a detailed study on the damage modeling of the electroformed copper is ongoing.

Acknowledgments

This research has been supported by the Italian Ministry of University and Research (MIUR), in the frame of the Hyprob project.

References

1. V. Salvatore et al., Design and Development of a LOX/LCH4 Technology Demonstrator, in *48th AIAA/ASME/SAE/ASEE Joint Propulsion Conference & Exhibit*, 30 July-01 August, Atlanta, Georgia (2012)
2. D. Haeseler et al., Green Propellant Propulsion Concepts for Space Transportation and Technology development Needs, in *ESA SP-557, Proceedings of the 2nd International Conference on Green Propellants for Space Propulsion*, 7-8 June, Cagliari, Sardinia, Italy (2004)
3. D. Haeseler, C. Mading, A. Gotz, V. Roubinski, S. Khrissanfov, and V. Berejnoy, Recent Developments for Future Launch Vehicle LOX/HC Rocket Engines, in *6th International Symposium Propulsion for Space Transportation of the XXIst Century, AAAF-02-100*, 13-17 May, Versailles, France (2002)
4. J. Collins, E. Hurlbert, K. Romig, J. Melcher, A. Hobson, and P. Eaton, Sea-Level Flight Demonstration & Altitude Characterization of a LO2/LCH4 Based Ascent Propulsion Lander, AIAA paper 2009-4948 (2009)
5. F. Battista et al., Development of a LOX/LCH4 Technology Demonstrator Based on Regenerative Cooling Throughout Validation of Critical Design Aspects with Breadboards in the Framework of the Hyprob Program, in *63rd International Astronautical Congress, IAC-2012*, Naples, Italy (2012)
6. C.D. Brown, Conceptual Investigations for a Methane-Fueled Expander Rocket Engine, AIAA paper 2004-4210 (2004)
7. ECOSIMPRO User's Guide, EA Internacional, Magallanes, Madrid, Spain
8. G.P. Sutton and O. Biblarz, *Rocket Propulsion Elements*, Wiley, New York, 2010, ISBN 9780470080245
9. D.K. Huzel and D.H. Huang, *Modern Engineering for Design of Liquid-Propellant Rocket Engines*, Vol 147, AIAA, Boston, 1992
10. W.H. Amstrong, Structural Analysis of Cylindrical Thrust Chambers, vol. 1. NASA technical report, 01 March 1979
11. H.I. Immich, J. Alting, J. Kretschmer, and D. Preclik, Technology Developments for Thrust Chambers of Future Launch Vehicle Liquid Rocket Engines, *Acta Astronaut.*, 2003, **53**, p 597–605
12. H.C. de Groh III and D.L. Ellis, Comparison of GRCop-84 to Other High Thermal Conductive Cu Alloys, NASA/TM—2007-214663 (2007)
13. G.A. Malone et al., Improved Electroformed Structural Copper and Copper Alloys, NASA/CR1998-208680
14. E. Kirner, D. Thelemann, and D. Wolf, Development Status of the Vulcain Thrust Chamber, *Acta Astronaut.*, 1993, **29**(4), p 271–282 ((ISSN 0094-5765))
15. O. Knab et al., Advanced Cooling Circuit Layout for the VINCI Expander Cycle Thrust Chamber, AIAA 2002-4005
16. H.J. Kasper and J.J. Notardonato, Effect of Low-Stiffness Closeout Overwrap on Rocket Thrust-Chamber Life, NASA technical paper 1456, May 1979
17. M. Ferraiuolo, W. Petrillo, and A. Riccio, On the Thermo-Structural Response of a Composite Closeout in a Regeneratively Cooled Thrust Chamber, *Aerosp. Sci. Technol.*, 2017, **71**, p 402–411
18. G. Henson, Chapter 7: Materials for Launch Vehicle Structures, 20170001809
19. J.R. Riccius, O.J. Haidn, and E.B. Zametaev, Influence of Time Dependent Effects on the Estimated Life Time of Liquid Rocket Combustion Chamber Walls, in *AIAA 2004-3670, 40th AIAA/ASME/SAE/ASEE Joint Propulsion Conference*, July 2004, Fort Lauderdale, Florida
20. R.G. Thiede, J.R. Riccius, and S. Reese, Life Prediction of Rocket Combustion-Chamber-Type Thermomechanical Fatigue Panels, *J. Propuls. Power*, 2017, **33**(6), p 1529–1542
21. N. Ozisik, *Heat Conduction*, Wiley, New York, 1980, https://doi.org/10.1002/aic.690260528
22. B.A. Boley and J.H. Weiner, *Theory of Thermal Stresses*, Dover Publications, New York, 1960
23. O. Golan et al., The Applicability of Norton's Creep Power Law and Its Modified Version to a Single-Crystal Superalloy Type CMSX-2, *Mater. Sci. Eng. A*, 1996, **216**(1–2), p 125–130 ((ISSN 0921-5093))
24. V.K. Arya and S.M. Arnold, Viscoplastic Analysis of an Experimental Cylindrical Thrust Chamber Liner, *AIAA J.*, 1992, **30**(3), p 781–789
25. J.R. Riccius, M.R. Hilsenbeck, and O.J. Haidn, Optimization of Geometric Parameters of Cryogenic Liquid Rocket Combustion Chambers, in *37th AIAA/ASME/SAE/ASEE JPC, AIAA-01-3408* (2001)
26. J.F. Maire and J.L. Chaboche, A New Formulation of Continuum Damage Mechanics (CDM) for Composite Materials, *Aerosp. Sci. Technol.*, 1997, **1**(4), p 247–257
27. M. Ferraiuolo, V. Russo, and K. Vafai, A Comparative Study of Refined and Simplified Thermo-Viscoplastic Modeling of a Thrust Chamber with Regenerative Cooling, *Int. Commun. Heat Mass Transf.*, 2016, **78**, p 155–162
28. J.C. Simo and T.J.R. Hughes, *Computational Inelasticity*, Springer, Berlin, 1998, ISBN 978-0-387-22763-4
29. R. Hetnarski and M. Eslami, *Thermal Stresses: Advanced Theory and Applications*, Springer, Dordrecht, 2009, ISBN 978-1-4020-9246-6
30. E. Thornton, Thermal Structures for Aerospace Applications, *AIAA Educ. Ser.*, 1996, https://doi.org/10.2514/4.862540
31. D. Cardillo et al., Numerical Simulation of a Lo2-Ch4 Rocket Engine Demonstrator, in *65th International Astronautical Congress, at Toronto, Canada*
32. J.J. Esposito and R.F. Zabora, Thrust Chamber Life Prediction: Mechanical and Physical Properties of High Performance Rocket Nozzle Materials, NASACR-134806, Contract NAS3-17838 (NASA-Lewis Research Center, Cleveland, 1975)
33. J.S. Porowski, W.J. O'Donnell, M.L. Badlani, and B. Kasraie, Simplified Design and Life Prediction of Rocket Thrust Chambers, *J. Spacecr. Rockets*, 1985, **22**(2), p 181–187